Chapter 5

Evolution of CB-like microstructure in $LiNdTiO_3$ based perovskites, and its effect on electrochemical properties

5.1 Introduction

A-site deficient perovskites containing Li^+-ions have received much attention due to their significant Li^+ conductivity. Among all, $Li_{3x}La_{(2/3)-x}\square_{(1/3)-2x}TiO_3$ x~0.16 (LLaTO) is the best with ionic conductivity of the order of 10^{-3} Scm^{-1} as it was first reported by Inaguma et al. [1]. This high conductivity is reported to originate from the existence of an optimum ratio of stable sites for Li^+ ion and vacancies. In addition, the Li^+-ions and the vacancies are connected by a shortest path way in combination with a bottleneck that is larger than the ionic diameter of Li^+(1.18Å) [2]. In perovskites, "bottleneck," is located in the space between two adjacent A-sites which is surrounded by four oxygens (in cubic lattice with space group Pm3m, corresponding to 3c site when B-site ion occupies the 1a site) [3]. Modification in the crystal structure by any means leads to a variation in six of bottlenecks, and if somehow, it becomes large enough to let the Li^+-ion flow smoothly through a shortest route, the ionic conductivity improves significantly [4]. For instance, in $La_{0.5}Li_{0.5}TiO_3$ substitution of other lanthanide ions (Ln = Pr, Nd, and Sm) with a smaller ionic radius than La decreases the bottleneck diameter that decreases ionic conductivity significantly. On the other hand, the substitution of Sr with a larger ionic radius than La increases the bottleneck diameter and ultimately improves the ionic conductivity [5].

Minimum charge recombination is also needed for improved electrochemical properties desired for battery application. It is possible to fabricate a microstructure consisting of well-separated Li conducting phase and Li lean phase to provide separate charge carrier transportation pathways. Such microstructure demands uniform, very finely dispersed domains at nanoscale. The smaller the size of the individual domains (or the wavelength, λ, of composition modulation), larger would be the interface area between the phases, and more efficient would be the charge percolation [6]. Such microstructures can be fabricated by bottom-up techniques or top-down approach through phases transformations. Spinodal decomposition is one of those techniques by which such microstructures consisting of coexisting Li-rich and Li-lean phases inter-twinned in a well-organized fashion can be designed. The evolution of chessboard-like microstructure in lanthanide-based perovskites ($LiLnTiO_3$, Ln= La, Nd, Pr etc.) appears to have most of the above-mentioned characteristics that would exhibit superior electro-chemical behavior from its bulk counterpart. CB microstructure in $LiLnTiO_3$ was first noticed by Guiton et al. [7][8]. They proposed the formation of nanoscale twin assisted CB-like structure in $(Ln_{2/3-x}Li_{3x})TiO_3$

perovskite systems. The CB-like microstructure that evolves in $LiNdTiO_3$ system, comprises of well-defined periodic nanoscale patterning of domains of tentatively $Nd_{2/3}TiO_3$ and $Li_{0.5}Nd_{0.5}TiO_3$ composition. $(Ln_{2/3-x}Li_{3x})TiO_3$ is well known to embrace alternative layers of fully occupied lanthanide and partially occupied mixed layers containing lanthanide, lithium cations, and vacancies along [001] as primary ordering. In addition, alternate mixed layer shows secondary ordering by switching positions of Li and Nd ions. The combined primary and secondary ordering results in a complex two-dimensional array of compositionally twinned and anti-phase boundaries. LLnTOs are reported to be prone for cationic ordering. They show prevalent A-site cationic ordering. Cationic ordering at A-site influences the coordination atmosphere of each neighbouring ion. For the cationic arrangement in poly-morphs of LLaTO, Harada et al. [9] defined the ordering parameter as $S = [R(\text{La-rich}) - R(\text{dis})]/[1-R(\text{dis})]$, where R(La-rich) and R(dis) are the occupancies of the A-sites by La^{+3} ions in (001) planes in the La-rich layer of the ordered form and La^{+3} ions occupancies in the dis-ordered form, respectively. For an ordered LLnTO system, Inaguma et al.[10] modified the above-mentioned relationship of ordering parameter (S), according to them the degree of ordered arrangement of La ions along the c-axis can be represented by, $S = ([R(\text{La-rich}) - R(\text{La-poor})]/[2 - R(\text{La-rich}) - R(\text{La-poor})])$, defined by, where R(La-rich) and R(La-poor) are the occupancies of the La^{+3} ions in the La-rich and La-poor ordered layers. Since the LLaTO and LNdTO are comparable systems, the relationship of ordering parameter (S) should be equally valid for LNdTOs. An increasing Li-ion content (increasing x) or temperature in the crystal structure reduces the ordering parameter in the crystal structure; simultaneously, the degree of orthorhombic distortion decreases.

These structural complexities can further enhance polymorphic phase transition, which modifies the crystal structure of the phases present in the microstructure. Robertson et al. reported a phase diagram study of the $(Li_{0.5-3x}RE_{0.5+x})TiO_3$ (RE=La, Nd) systems that explained the polymorphic transformations in both the $(Li_{0.5-3x}La_{0.5+x})TiO_3$ and $(Li_{0.5-3x}Nd_{0.5+x})TiO_3$ systems. It is reported that La based systems can form three polymorphs A (cubic), α (tetragonal, double perovskite unit cell), β (tetragonal). While, Nd based systems show four polymorphs A (primitive cubic), α′ ($\sqrt{2}a$, $\sqrt{2}a$, 2a-δ tetragonal, where δ is small distortion), C (orthorhombic distortion of α′), and β ((a, a, 2a+Δ) tetragonal where Δ is large distortion). Phase diagram of $LiNdTiO_3$ explains that with a continuous decrease in temperature (1400 ℃ to 800 ℃) system adopts a continuous symmetry breaking polymorphic transition from A to C (cubic to orthorhombic), C to α′ (orthorhombic to tetragonal) and α′ to β (tetragonal to tetragonal) [11]. Combined with these phase transformation complexities, spinodal decomposition gives birth to the nano chessboard-like microstructure consisting of 3D well-organized alternative domains [7]. This 3D alternative distribution of Li-rich and Li-lean phases are expected to provide separate channels for the un-interactive flow of charge and holes. However, Erni et al. and Azough et al. have contradicted the compositional phase separation by correlative microscopy [12][13]. On the basis of high-resolution HAADF-STEM-EDS data supported with corresponding EELS spectrum, they have explained that CB like contrast is the consequence of BO_6 octahedral tilting and incommensurate modulation of strained lattice. The substitution of aliovalent cations and vacancy distribution at A-site accounts for the variation in the Ti-O bond lengths [12]. The difference in six Ti-O bond lengths introduces significant distortion in the unit cell, which provides a off-center shift to Ti^{+4} cations resulting in octahedral TiO_6 tilting [14]. Hence, a cumulative effect of cation ordering at A-site and TiO_6 tilting is responsible for the variation in the lattice parameters [2]. This site-specific cationic ordering administers tilting of the BO_6 octahedra along some specific directions. A well-defined tilting of BO_6 octahedra affects the O-O distance in those specific directions. Ultimately, The enlargement of O-O bond increases the bottleneck diameter, which favors diffusion of Li-ions along these specific crystallographic directions [15]. Considering all the aforementioned rationalities, it can be concluded that ionic conductivity of LLnTO is subjected to various factors such as compositional phase separation, octahedral tilting, cationic ordering, lattice parameters and grain boundary effects, etc. All these factors affect the Li-ion-transportation in LLnTOs. To understand the mechanism of Li^+-ions transportation in LLnTOs and develop the novel solid-state electrolytes (SSEs) with improved electrochemical properties, a study of correlation between these parameters is of great importance. Although, there are reports correlating the electrochemical properties of LLnTOs with their crystal structures [16]. Up to the best of knowledge of the author, there is hardly any report that provides a comparative study of the electrochemical properties of bulk and CB-like microstructure developed in any system. In this study we have tried to elucidate the mechanism of CB-like microstructural evolution in a $LiNdTiO_3$ system, and its effect on electrochemical properties. A transmission electron microscopy (TEM) and atom probe tomography (APT) based correlative investigation has been carried out in order to contribute in a long-standing debate, whether evolution of CB microstructure in LLnTOs involves a compositional phase separation or it is totally a structural phenomenon. All the investigations were performed on $Li_{3x}Nd_{(2/3)-x}\square_{(1/3)-2x}TiO_3$ samples, a rare class of perovskites containing Nd atom along with a high percentage of vacancies and highly mobile Li-ion on A-site.

5.2 Materials and methods

LLnTO compounds with a generalized stoichiometry $Li_{3x}Nd_{0.5}\square_{0.5-3x}TiO_3$ was prepared by solid-state synthesis route due to its ease of materials handling and success probability. In this compound, lithium stoichiometry was systematically varied between $0.16 > x > 0.05$, so as to obtain the compounds with nominal composition $Li_{0.15}Nd_{0.5}TiO_3$, $Li_{0.24}Nd_{0.5}TiO_3$, $Li_{0.36}Nd_{0.5}TiO_3$ and $Li_{0.48}Nd_{0.5}TiO_3$ to cover a wide portion of phase diagram that shows high probability of phase transitions. For x ~0.16, it forms a perfect electrically neutral crystal, for $x < 0.16$, it should form oxygen vacancies and for $x > 0.16$, it should form A-site excess structure. The chosen compositions are all 'A' site deficient or oxygen vacant perovskites. Ultra-pure precursor powders of Nd_2O_3, TiO_2 and Li_2CO_3, each more than 99.99% purity (Sigma Aldrich & Alfa Aesar) were mixed and pelletized in stoichiometric proportions to obtain the mixed oxides with the above-mentioned compositions. The green pellets were sintered in air at 1250 °C for 24 hours followed by cooling through two different routes. One set of samples were subjected to annealing by furnace cooling at ~10 °C/hour and the another set of samples were quenched on a cold surface with simultaneous blow of air. In order to prevent the lithium loss during heat treatments, pellets of similar composition were stacked vertically and the sandwiched pellets were taken for further analysis.

(a) Microstructural characterizations

Heat treated and annealed/normalized samples were structurally characterized by X-ray diffraction in a Panalytical Empyrean high-resolution X-ray diffractometer operated at 40 kV with 40 mA current. For X-ray diffraction experiments Co-K_α radiation with wavelength of 1.78 Å was used. For accurate analysis of the crystal structures, the X-ray diffraction patterns were Rietvelt refined using FullProf software. For transmission electron microscopy (TEM) observations, slices were obtained from the sintered and annealed/normalized pellets and then ground separately into powder. For each TEM sample, the powder was suspended in ethanol and was subjected to ultrasonication for about

20 minutes before it was drop cast onto a carbon coated copper grid. TEM observations were made at 200 kV in a Tecnai G^2 T20 transmission electron microscope. The reconstruction of the crystal structure was done on Vesta software by utilising the CIF generated from Rietvelt refinement of the XRD patterns.

(b) Electrochemical characterizations

The electrochemical performance of all the $LiNdTiO_3$ samples was estimated against the Li reference electrode. Working electrodes for each sample were prepared by mixing corresponding powders, PVDF, and carbon black in 8:1:1 weight ratio. Further NMP: N-Methyl-2-pyrrolidone was added to make a slurry of the mixture. This slurry was coated onto a copper substrate. This coated Cu substrate was allowed to dry at 1000 °C to evaporate the solvent. The electrochemical analysis of each prepared sample was performed against lithium metal with a coin type 2032 cell utilizing a non-aqueous electrolyte (1M LiPF6/EC: DMC=1:1 in volume) and a polypropylene separator (Celgard 3501). This process was done in the glovebox back filled with high purity argon to avoid contamination. Cyclic voltammograms were generated within the voltage range of 0.01–3V (vs. Li/Li^+) at the scan rate of $0.2mVs^{-1}$ at 25°C.

(c) 3D tomographic re-construction

To prepare the tip for APT characterization, pre-characterized CB-samples were taken into account, and needle-shaped specimens were lifted out from vintage sites using a dual beam workstation SEM–FIB (FEI Helios Nanolab G4UX). The process is explained stepwise in Chapter 2 (Figure 2.4). To minimize the Ga^+ beam damage, a low-energy milling step (5 keV) was used at the final stage of sample preparation. APT measurements were performed in pulsing laser mode (wavelength of 355 nm (UV)) on Local Electrode Atom Probe (LEAP) 5000 XR, Cameca Instruments. During the whole process, the tip temperature was maintained at 60 K. The laser pulse frequency was set to 250 kHz with 30 pJ energy. The data collection rate was 0.5% ions per field evaporation pulse. The microstructural reconstruction and data analysis were performed on the Integrated Visualization and Analysis Software (IVAS 3.8.10) of Cameca Instruments Inc (Madison, WI, USA).

5.3 Result and discussion

5.3.1 Microstructural characterization

LLnTOs are very prone to polymorphic phase transformations, hence for a small variation in physical conditions often they transform into structurally related phases. These phases are reported to be very similar to each other, hence a very precise characterisation is needed to distinguish them and to know their morphology in the microstructure.

5.3.1.1 XRD analysis

Figure 5.1 (a) shows the X-ray diffraction patterns of the $\mathrm{Li}_{3x}\mathrm{Nd}_{0.5}\square_{(1/3)-2x}\mathrm{TiO}_3$ sample sintered at 1250°C for 24 hours followed by annealing at a cooling rate of ~10 °C/hour. The lithium content in the sample has been varied by x = 0.05, 0.08, 0.12 and 0.16 so as to obtain the compositions $\mathrm{Li}_{0.15}\mathrm{Nd}_{0.5}\mathrm{TiO}_3$, $\mathrm{Li}_{0.24}\mathrm{Nd}_{0.5}\mathrm{TiO}_3$, $\mathrm{Li}_{0.36}\mathrm{Nd}_{0.5}\mathrm{TiO}_3$ and $\mathrm{Li}_{0.48}\mathrm{Nd}_{0.5}\mathrm{TiO}_3$.

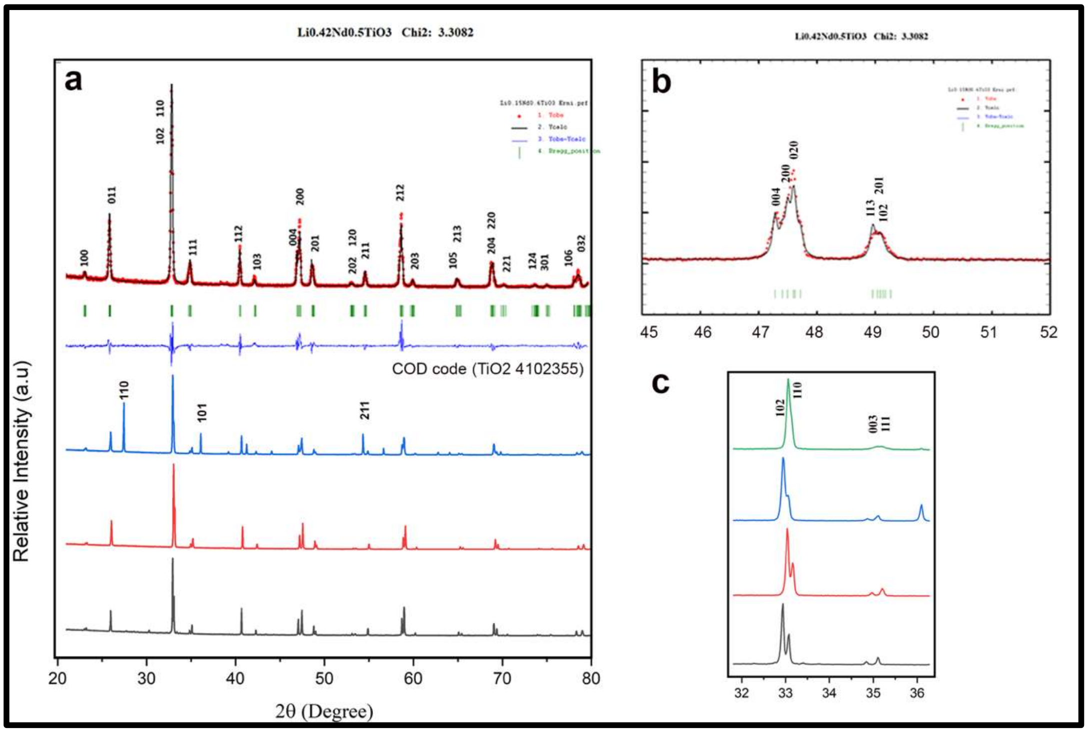

__Figure 5.1:__ XRD patterns of $\mathrm{Li}_{3x}\mathrm{Nd}_{(2/3)-x}\square_{(1/3)-2x}\mathrm{TiO}_3$ samples after sintering at 1250 °C followed by annealing in air atmosphere (a) stack of XRD pattern for x = 0.05, 0.08, 0.12 and 0.16, sequentially form bottom to top (b) magnified view of Rietveld refined XRD pattern corresponding to x = 0.16 in a 2θ range from 45° to 52° and (c) a magnified view of stacked patterns for all four values of x in a 2θ range from 32° to 36°.

All the diffraction patterns approximately match with $Li_{0.5}Nd_{0.5}TiO_3$ structure. However, there are finer details available in the diffraction patterns that point out to crucial modifications in crystal structures. To study these finer details, all the diffraction patterns were Reitveld refined. The pattern at the top of Figure 5.1(a) shows Reitveld refined diffraction pattern of $Li_{0.48}Nd_{0.5}TiO_3$ sample sintered at 1250 °C followed by annealing to room temperature. In this pattern clear splitting in many of its major peaks, i.e., 110, 200, 212 and 204 is observed. The zoomed-in version of the 110 peaks in Figure 5.1(c) indicates that for $Li_{0.15}Nd_{0.5}TiO_3$ and $Li_{0.24}Nd_{0.5}TiO_3$ samples, this peak is clearly split into 110 and 012 or 102. The same split is not so much evident for $Li_{0.36}Nd_{0.5}TiO_3$ and $Li_{0.48}Nd_{0.5}TiO_3$. However, a clear shoulder is observed for the same peak in $Li_{0.36}Nd_{0.5}TiO_3$ and $Li_{0.48}Nd_{0.5}TiO_3$. The shouldering and splitting clearly indicates the variation in lattice parameters due to cation ordering in these directions and most likely the ordering tendency increases with the decrease in lithium content in the oxide. This necessarily indicates a cubic to tetragonal transformation in this perovskite and the doubling of the 'l' parameter of the indices refers to the doubling of lattice parameter along c-direction due to ordering. In a similar line, the zoomed-in version of Rietveld refined 200 peak of $Li_{0.48}Nd_{0.5}TiO_3$ (Figure 5.1(b)) also shows similar split into 004 and 200 or 020. This observation also refers to a cubic to pseudo-tetragonal transformation with approximate doubling in the c-parameter due to ordering. Additionally, a minor split between 200 and 020 can also be observed in Figure 5.1(b), which may refer to the presence of the same phase with orthorhombic structure. However, extent of split necessarily indicates very little orthorhombicity. Similarly, split in the 212 and 204 peaks (Figure 5.1(a)) reinforces the idea of cubic to tetragonal transformation due to ordering in the c-direction of the lattice. The agreement between the observed and refined XRD patterns in Figure 5.1(a) refers to a pseudo-tetragonal β-phase with a_p x ~a_p x $2c_p$ unit cell here $a_p \sim 3.82$ Å, $a_p \sim 3.84$ Å and $c_p \sim 7.68$ Å. Similar phase has been reported before. Additionally, some extra peaks in the XRD pattern of $Li_{0.36}Nd_{0.5}TiO_3$ at $2\theta = 27$, 36 and 54 degrees are noticed (Figure 5.1(a)). These peak positions indicate the presence of tetragonal TiO_2 as a separate phase in the microstructure. Similar peaks with very small intensities are also observed in $Li_{0.48}Nd_{0.5}TiO_3$, which may be associated with the presence of TiO_2 phase in minute volume fraction. The three XRD patterns of the differently treated $Li_{0.48}Nd_{0.5}TiO_3$ sample, i.e., sintered and quenched, sintered and annealed, sintered and annealed followed by running 100 charging and discharging cycles, were compared in Figure 5.2(c), 5.2(b), and 5.2 (a), respectively. The XRD pattern of $Li_{0.48}Nd_{0.5}TiO_3$ sample after sintering and quenching

(Figure 5.2(c) matches to a orthorhombic perovskite structure with Pnma space group with lattice parameter a_o~5.43 Å, b_o~5.41 Å and c_o~7.66 Å.

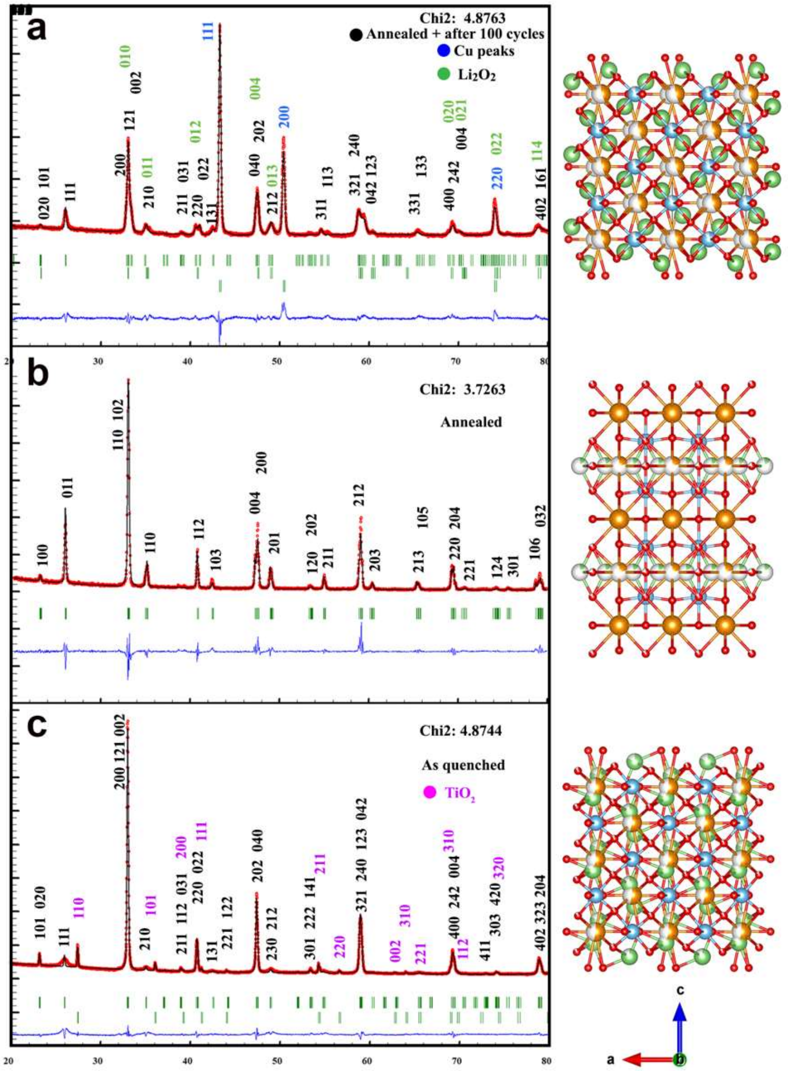

Figure 5.2: *Rietveld refined XRD patterns of* $Li_{0.48}Nd_{0.5}TiO_3$ *sample (a) after sintering at 1250 ℃ follow by annealing and running 100 cycles of charging and discharging. This structure matches with an orthorhombic perovskite structure with Pnma space group (*a_o*~5.45 Å,* b_o*~5.36 Å and* c_o*~7.67 Å.) (b) after sintering at 1250 ℃ followed by annealing. The structure matches to psudotetragonal (orthorhombic) with very minute difference in a and b lattice parameters ~* $a_p \times a_p \times 2c_p$ *(3.82 Å x 3.81 Å x 7.68 Å) that may considered as to tetragonal lattice with P4/mmm symmetry (c) after sintering at 1250 ℃ followed by quenching. The structure matches to an orthorhombic structure (*$\sqrt{2}\,a_p \times \sqrt{2}\,a_p \times 2c_p$*, 5.43 Å x 5.41 Å x 7.66 Å) with Pnma space group.*

The pattern in Figure 5.2(b) is related to the same sample but after sintering and annealing for prolonged hours (10°C/hours), which matches to a pseudo-tetragonal β-phase with a_p x ~a_p x $2c_p$ unit cell here $a_p \sim 3.82$ Å, $a_p \sim 3.84$ Å and $c_p \sim 7.68$ Å. It is incorporated in this stack as a reference pattern to juxtapose XRD patterns obtained after various treatments such as running charging and discharging cycles and quenching, in order to more readily distinguish the structural modifications. The pattern in Figure 5.2(c) is related to the sintered and annealed $Li_{0.48}Nd_{0.5}TiO_3$ sample after running 100 charging and discharging cycles between the potential range 0.01 to 3V. This pattern matches with similar orthorhombic perovskite structures with Pnma space group with lattice parameter $a_o \sim 5.45$ Å, $b_o \sim 5.36$ Å and $c_o \sim 7.67$ Å. The comparative study between the patterns in Figure 5.2(a) and Figure 5.2(b) shows that the splitting in the major peaks is almost absent in the quenched sample, which is indicative of negligible ordering between the Li and Nd-ions at the A-site of the perovskite lattice. Higher temperature is favorable for diffusion of cations. During annealing, longer residence time at higher temperatures allows the cations to diffuse to a suitable low energy A-site, which is a factor, that should favor the development of order. However, the absence of strong ordering in the quenched sample may be explained in the light of its residence time at high temperature. During quenching, as the residence time at the higher temperature is short, ordering is not promoted and the structure remains in a relatively disordered orthorhombic state. Additionally, minute volume fraction of TiO_2 phase also may be present in this sample. The XRD pattern in Figure 5.2(c), i.e., after running 100 charging and discharging cycles shows some extra peaks at $2\theta = 43$, 51 and 74 degrees, which can be associated with Cu substrate, which is used for electrochemical studies. The split in 110, 112 and 212 peaks are still observed after 100 charging and discharging cycles, which signifies structural stability and the existence of order in the structure. The extent of split in the peaks in Figure 5.2(c) is considerably well developed as compared to the pattern in Figure 5.2(b). This signifies that after 100 charging and discharging cycles either the ordering has been enhanced or two different structures with quite similar lattice parameter has developed. This might arise out of minor compositional variation, which warrants for further investigation. It is found out that after the charging and discharging cycles additional hexagonal Li_2O_2 phase with $P\overline{6}$ space group (a = 3.13 Å, b =3.13 Å and c = 7.64 Å) is also formed as indexed in Figure 5.2(a).

5.3.1.2 TEM analysis

To further elucidate the structural and morphological aspects of sintered and annealed $Li_{0.48}Nd_{0.5}TiO_3$ sample, TEM BF images and corresponding electron diffraction patterns are given in Figure 5.3(a-f). In the BF image in Figure 5.3(a), cross penetration of linear fringes (Zoomed in version of area marked by white dotted square) leading to the formation of square domain like structure is observed. The size of the domains is ~ 4nm X ~ 4nm. The corresponding electron diffraction pattern (Figure 5.3(d)) taken along $[11\bar{1}]$ zone axis indicates ordering along 110, 112 and 202 direction, which is in agreement with the split of peaks in the X-ray diffraction pattern for the same sample in Figure 5.1(a).

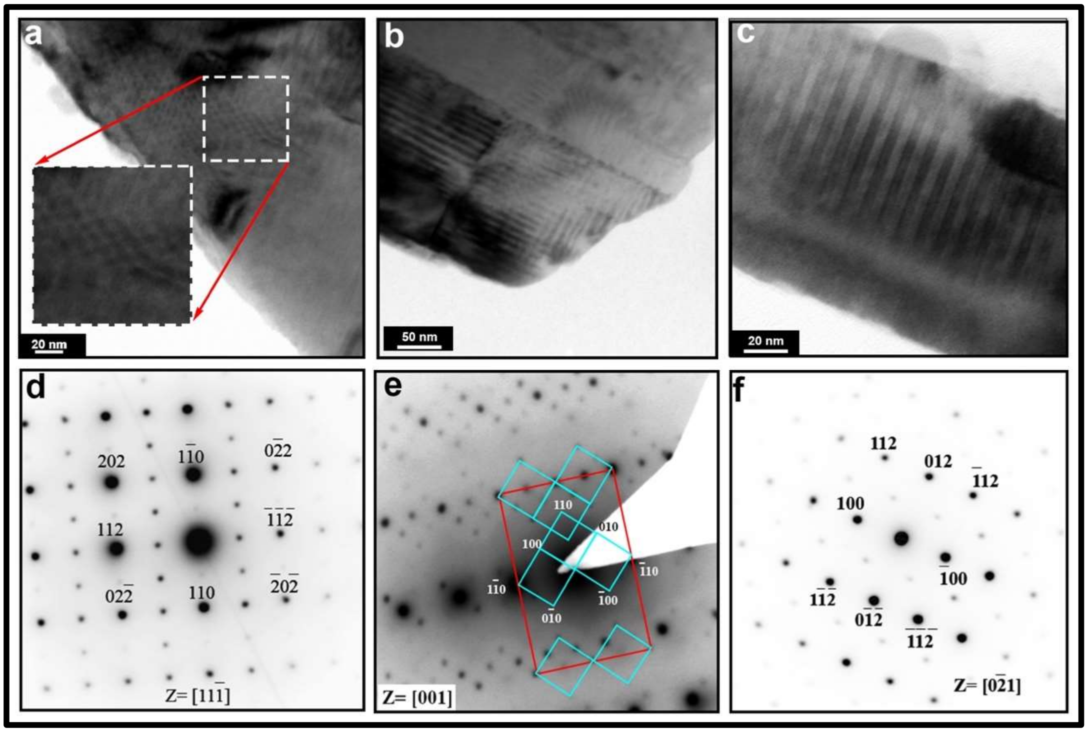

Figure 5.3: *Electron micrographs of* $Li_{0.48}Nd_{0.5}TiO_3$ *sample after sintering at 1250 °C for 24 hours followed by annealing, bright field image and corresponding electron diffraction pattern along (a, d)* $[11\bar{1}]$, *(b, e)* $[001]$ *and (c, f)* $[0\bar{2}1]$ *zone axis.*

This superlattice reflections further reinforces the idea of ordering induced doubling of lattice parameter in c-direction in the pseudo-tetragonal lattice of sintered and annealed sample of $Li_{0.48}Nd_{0.5}TiO_3$. In the TEM BF-image from a different region of the same sample (Figure 5.3(b)) perpendicular fringe pattern with ~ 4nm X~ 4nm domain size could be observed. Rotationally oriented diffraction pattern from this region (Figure 5.3(e)) shows that the domains are having interfaces along 100 and 010 planes.

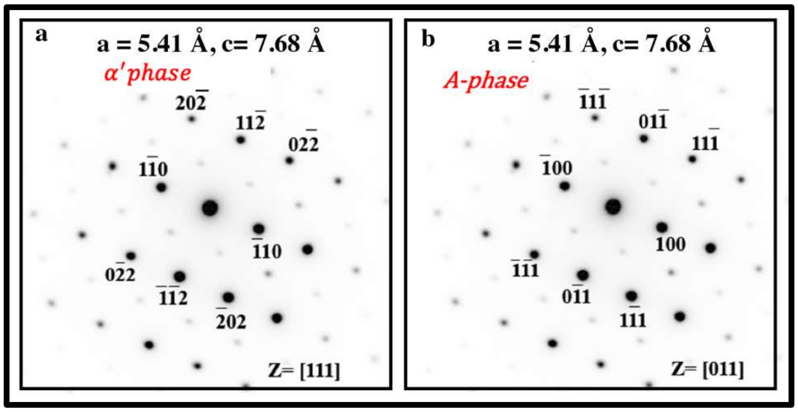

Figure 5.4: *Electron diffraction pattern of* $Li_{0.48}Nd_{0.5}TiO_3$ *sample after sintering at 1250 °C for 24 hours followed by quenching and annealing considering (a) orthorhombic α′ phase with a = 5.41 Å, c = 7.68 Å along [111] zone axis (b) cubic A-phase with a = 3.83 Å along [011] axis.*

In this diffraction pattern extra spots are visible along 100, 010 and 110 direction. Ordering along 100 and 010 is contrary to the x-ray diffraction pattern of the same sample and it will be explained in the subsequent section. In the BF image from the same sample (Figure 5.3(c)) linear fringe contrast with ~4nm width could be observed. The rotationally oriented diffraction pattern of the same region (Figure 5.3(f)) indicates that the interfaces in the BF image (Figure 5.3(c)) are along 100 planes. The diffraction pattern (Figure 5.3(f)) can be indexed in three ways: Z = $[0\bar{2}1]$ of pseudo-tetragonal β phase with a_p ~ 3.82 Å, a_p ~3.84 Å and c_p~ 7.68 Å; Z=$[11\bar{1}]$ of orthorhombic α′ phase with a_o~5.43 Å, b_o~5.41 Å and c_o~7.66 Å (Figure 5.4(a)); Z=[011] of cubic A-phase with a~3.83 Å (Figure 5.4(b)).

The ordering behavior observed from both the techniques TEM and XRD are falling in the same line, except in figure 5.5(d), where ordering in (100) and (010) planes is not consistent with the corresponding crystal structure a_p x a_p x $2c_p$ obtained by Reitveld refined XRD data. To resolve this discrepancy the difference in the intensities of superlattice reflections have been utilized. A critical observation of figure 5.5(d) shows that superlattice reflections along $[100]_p$ and $[010]_p$ directions are less intense than $[110]_p$ (p stands for primitive cubic perovskite cell). To further elucidate this discrepancy, reconstruction of the crystal structure is done with the CIF generated by Reitveld refinement of corresponding XRD patterns. Figure 5.5(a) shows the simulated crystal structure of the sintered and annealed $Li_{0.48}Nd_{0.5}TiO_3$ sample along [100] direction.

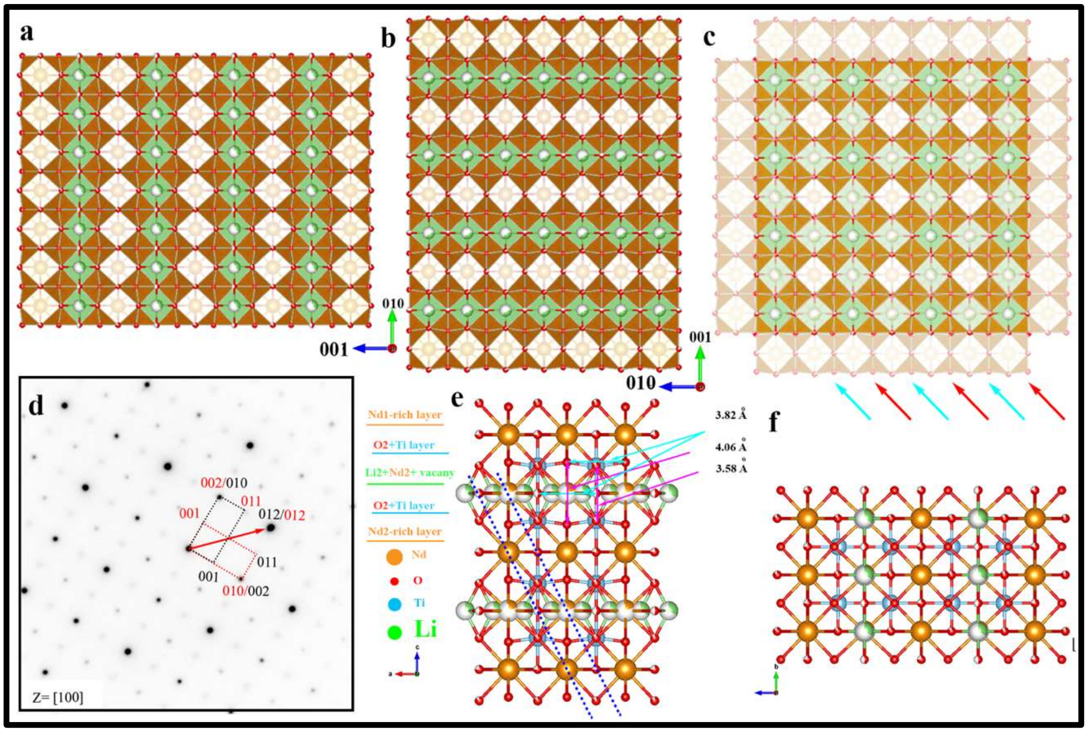

Figure 5.5: *Atomic structure of $Li_{0.48}Nd_{0.5}TiO_3$ sample after sintering at 1250 °C for 24 hours followed by annealing with (a) 100 as projection vector and 010 upward vector (b) 100 as projection vector and 001 as upward vector (c) the composite of (a) and (b). (d) electron diffraction pattern along [100] zone axis showing two separate ordered supercell marked in red and black (e) atomic arrangement in the crystal structure of single domain of $Li_{0.48}Nd_{0.5}TiO_3$ with 010 as projection vector and 001 as upward vector (f) 100 as the projection vector 010 as upward vector exhibiting ordering in (001) and (012) planes.*

In this figure 2D view of crystal structure with 100 projection vector shows ordering of Nd-rich and Nd-lean layers along [001] direction. Same crystal structure along same projection vector but with 90° rotation clock-wise direction is shown in Figure 5.5(b). The diffraction pattern in Figure 5.5(d) can be considered as a composite diffraction pattern when Figure 5.5(a) and Figure 5.5(b) are superimposed upon one another. Each such individual nanodomain consists of alternative Nd-rich and Li-rich layer in [001] direction (Figure 5.5 (a, b)). The overlaid resultant image is given in Figure 5.5(c). The electron diffraction pattern shown in the figure 5.5(d) is coming from a specific portion of the microstructure in such a way so that their ordered (001) planes are mutually perpendicular as shown in Figure 5.3(b). The corresponding diffraction pattern of these two perpendicular domains are marked as red and black dotted rectangles in composite electron diffraction pattern (figure 5.5(d)). In this composite electron diffraction pattern difference in the intensity of superlattice spot along 001, 011 and 012 can be related to overlaying of two diffraction pattern of two ordered orientation variants. The superlattice spots along [012] are more intense in compare to superlattice spots along [001] directions, because the superlattice spot along [012] is common for both the domains, and intensities of (012) planes of two orientation phase variants are superimposed (Figure 5.5(c)). While, superlattice spots along [001] and [010] directions are unique for each ordered orientation variants [17]. In addition, these ordered domains are twinned in (012) planes (marked as red arrow figure 5.5(d)). The superimposition of corresponding individual electron diffraction patterns results in a composite electron diffraction pattern as shown in Figure 5.5(d). On the other hand, the disordered solid solution of $Li_{0.48}Nd_{0.5}TiO_3$ does not show any ordering signature. Corresponding bright-field image form similar zone axis are not showing any feature of CB microstructure. Additionally, the tilting of the TiO_6 octahedra can also be responsible for introducing ordering along various directions [18].

5.3.1.3 3D reconstruction of microstructure by APT

The concentration profile of $Li_{0.48}Nd_{0.5}TiO_3$ sample was reconstructed through atom probe tomography (APT). Figure 5.6 represents iso-concentration surfaces of Nd and Li to visualize the compositional distribution of rod-like domains, appeared in TEM bright field images shown in Figure 5.3(c). A preferential view of APT tip and corresponding elemental map (along the arrowed direction) are shown in Figures 5.6(a) and 5.6(b), respectively. In Figure 5.6(a) an iso-concentration surface map of Nd atoms clearly depicts a periodic segregation of Nd atoms in 3D space, this periodic segregation of Nd atoms may also be corroborated by corresponding elemental concentration profiles shown in Figure 5.6 (b). In Figure 5.6 (b), complementary change in Ti and Nd concentration graphs denotes that the domains consist of different phases. The linear composition distribution profile indicates that the domains are ~7-10 nm in width. The Nd rich domains are lean in Li and Li rich domains are lean in Nd. As Nd and Li share similar A-site of the perovskite lattice this behavior can be correlated to their ordering and segregation. Li rich domains are found to be rich in Ti. This behavior can directly be correlated to the need to maintain the local electrical neutrality of the lattice. Similarly, Figures 5.6 (c, d) illustrates segregation of Li and Nd atoms.

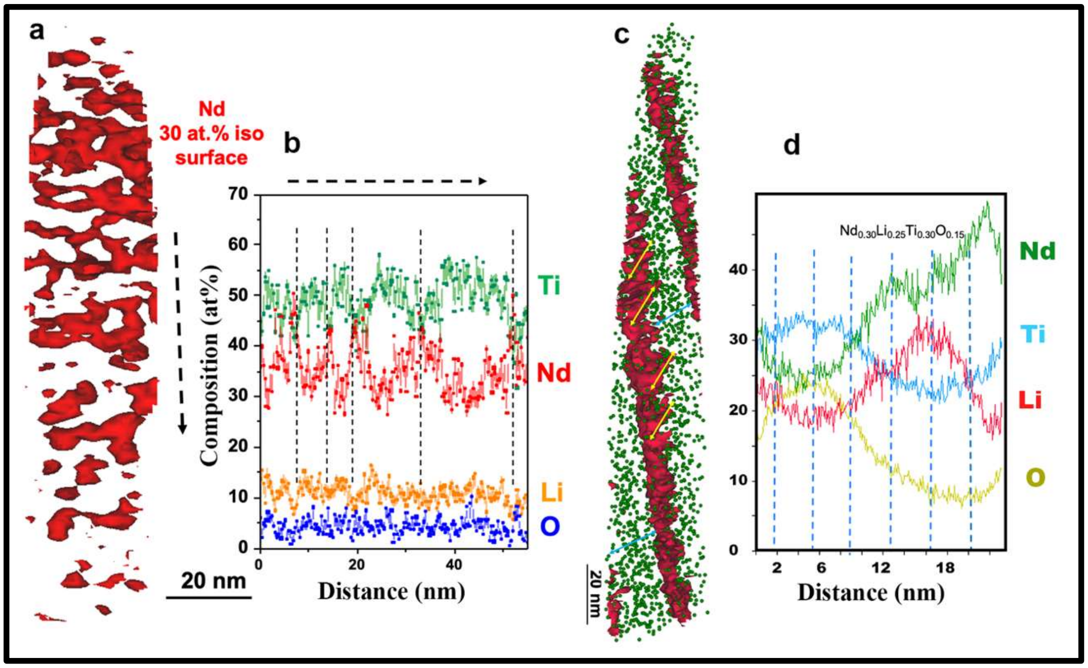

Figure 5.6: *3D elemental map of Li, Nd, Ti, and O in* $Li_{0.48}Nd_{0.5}TiO_3$*, represented by their respective iso-concentration surfaces with two different orientations (a-b) Nd iso-concentration surface map at 30 at% shows a complementary modulation of Ti and Nd concentration with a half wavelength of ~7nm-12nm (c-d) Li iso-concentration surface map at 28 at% in combination with Nd atomic position exhibits an alternative distribution of Li concentration.*

From the iso-concentration surface of Li, it can be clearly visualized that two separate phases are rich in Nd and Li concentrations. These results clearly reveal the elemental segregation in $Li_{0.48}Nd_{0.5}TiO_3$, where one phase is rich in Li^+. This finding provides a clear evidence of role of compositional phase separation in CB-like microstructural evolution in LLnTOs, and it may play a vital role in ending the long-standing debate (explained in Chapter1). In the microstructure of $Li_{0.48}Nd_{0.5}TiO_3$, an alternative distribution of Li-rich and Nd-rich phases may facilitate a channelized flow of Li-Ions.

5.3.2 Effect of CB-like microstructural evolution on electrochemical properties

To further characterize the effect of evolution of CB-like microstructure in $Li_{0.48}Nd_{0.5}TiO_3$ sample a correlation between the genesis of CB-like microstructure and electrochemical properties can provide a new perspective in the development of ASSLBs. In order to do that, electrochemical properties of $Li_{0.48}Nd_{0.5}TiO_3$ sample were compared before and after the development of CB-like microstructure. In addition, electrochemical properties of $Li_{0.48}Nd_{0.5}TiO_3$ and $Li_{0.36}Nd_{0.5}TiO_3$ samples have been compered after providing same heat treatment in order to know the effect of Li content on their performance. Figure 5.7 shows the voltammograms of $Li_{0.48}Nd_{0.5}TiO_3$ and $Li_{0.36}Nd_{0.5}TiO_3$ samples relating major electrochemical properties such as the current, specific capacity and columbic efficiency. Wherein, Figure 5.7(a) shows the voltammograms (current-voltage curves) corresponding to the sintered and annealed $Li_{0.48}Nd_{0.5}TiO_3$ sample in which CB-like microstructure (Figure 5.3(b)) evolved during the sintering at 1250 °C for 24 hours followed by a prolonged annealing (10 °C/hours). This cyclic voltammogram shows de-insertion and insertion of Li^+ ions in the voltage range from 3 to 0 V versus Li/Li^+, at a scanning rate of 0.2 mVs^{-1}. The lower half of this liner sweep voltammogram illustrate three cathodic (reduction) peaks in approximation of ~1.65 V, 0.6 V and 0.1V. These peaks exhibit electrochemical lithium insertion into the sample. In order to maintain the charge-neutrality in the structure an electron should be gained thus reduction of any of its elements is inevitable. Since in $LLnTO_3$, Ln ions does not participate in the redox reaction, an insertion of Li^+ ion in to the structure Ti^{+4} reduces to Ti^{+3}. In the redox reaction of such samples, peaks at less than 1V can be ascribed to the lithium insertion into acetylene black. Hence, 0.6 V and 0.1 V Peaks may be considered to be related to lithium insertion into the acetylene black [19]. In this process acetylene facilitates the mixed carbon that not only enhances the electronic conductivity in the sample sheet, but also provides catalytic-active places for the electrochemical reaction and diffusion of lithium ions [19]. On the other hand, upper half of the voltammogram shows four peaks at 0.1V, 0.7V, 1.35V and 1.75 V. Here also, peaks at 0.1 V and 0.7 V can be referred to as lithium desertion form acetylene black, while peaks at 1.35 V and 1.75 V are related to Li desertion from the $Li_{0.48}Nd_{0.5}TiO_3$ sample.

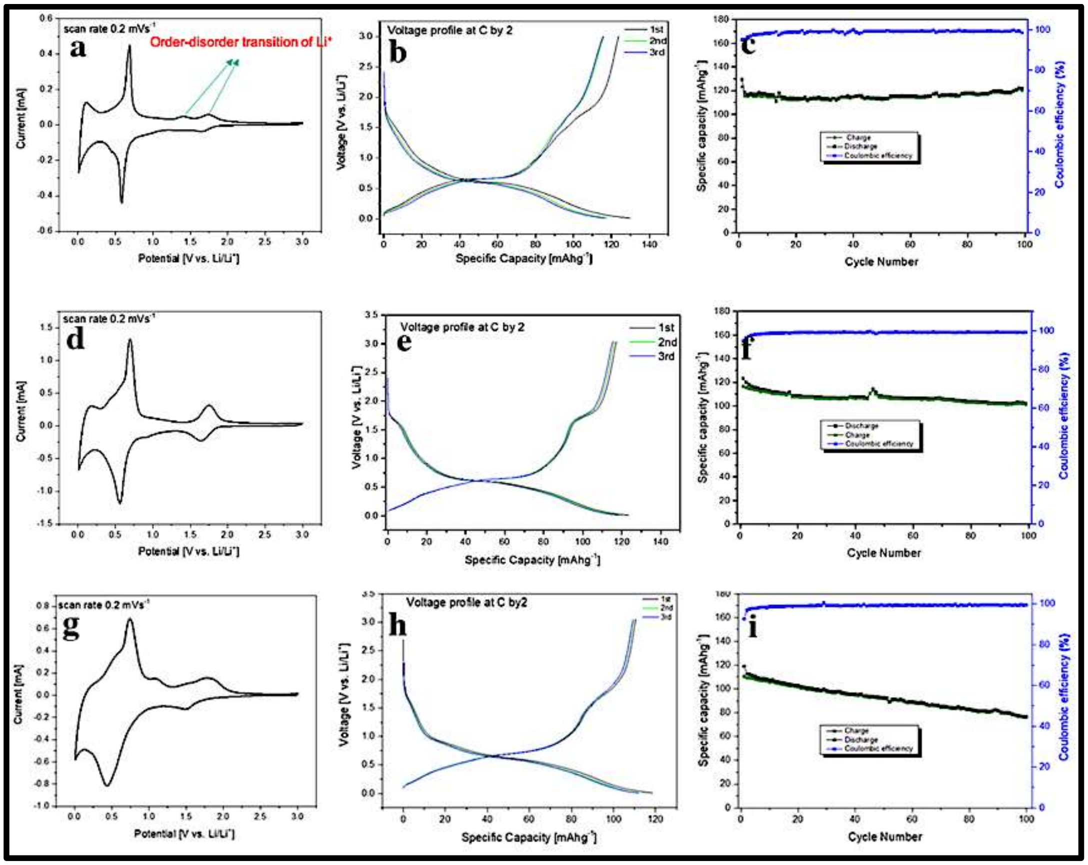

Figure 5.7: *Electrochemical graphs of a $Li_{0.45}Nd_{0.5}TiO_3$ sample after sintering at 1250 °C for 24 hours followed by quenching and annealing (a) voltammogram with a scan rate 0.2 mVs^{-1} showing order-disorder transition of Li^+*[20]*(b) voltage Vs Specific capacity (charge-discharge profile) at C/2 (c) Specific capacity Vs Cycle number Vs coulombic efficiency. (d, e, f) similar electrochemical graphs of $Li_{0.45}Nd_{0.5}TiO_3$ sample after sintering at 1250 °C for 24 hours followed by quenching. (g, h, i) similar electrochemical graphs of $Li_{0.35}Nd_{0.5}TiO_3$ sample after sintering at 1250 °C for 24 hours followed by annealing.*

The sintered-annealed $Li_{0.48}Nd_{0.5}TiO_3$ sample has an ordered structure, and ordering happens in 001 planes as the A-site of Li-rich and Li-lean layers fill up with different cations, its coordination atmosphere would be different for both the A-sites (Figure 5.7 (a)). Hence, redox peaks in the vicinity of ~ 1.75 V and ~1.35 V may be ascribed to the stepwise insertion/desertion of lithium into the different sites, e.g., ordered A-sites, 3C site, in the $LiNdTiO_3$ perovskite [19]. These two peaks refer to an order-disorder transition of Li^+ ion [20]. In comparison, there are only three peaks in the upper half of voltammogram of a sintered-quenched $Li_{0.48}Nd_{0.5}TiO_3$ sample, positioned at 0.15 V, 0.75 V and 1.75 V (Figure

5.7 (d)). Here also, peaks at 0.15 V and 0.75V can be correlated to lithium desertion from the acetylene black, while a single peak at 1.75 V refers to Li^+ ion desertion from the disordered A-site. Figures 5.6 (b, e) show the charge-discharge curves of both sintered-annealed and sintered-quenched $Li_{0.48}Nd_{0.5}TiO_3$ cathodes at a current rate of C/2, respectively. The oxidation curve of sintered and annealed $Li_{0.48}Nd_{0.5}TiO_3$ sample after running first cycle shows 130 mAhg^{-1} at 0 V, but it shows a reduced capacity 118 mAhg^{-1} in second cycle. Similarly, a reduction in the specific capacities from 125 to 115 mAhg^{-1} is observed at 3 V in the reduction curve. Moreover, Sintered-annealed and sintered-quenched $Li_{0.48}Nd_{0.5}TiO_3$ cathodes exhibited similar initial discharge capacities (118 mAh g^{-1} and 120 mAh g^{-1}). However, the specific capacity after the first and second cycles appears relatively consistent in the sintered-quenched $Li_{0.48}Nd_{0.5}TiO_3$ sample. Figures 5.7(c,f) exhibit cyclic performance of sintered-annealed and sintered-quenched $Li_{0.48}Nd_{0.5}TiO_3$ samples, respectively. The coulombic efficiencies and specific capacities of both the samples are almost equal in the beginning of the charging-discharging cycles, ~99% with a specific capacity (120 mAh g^{-1}). The specific capacity and coulombic efficiency of sintered-annealed $Li_{0.48}Nd_{0.5}TiO_3$ sample remain almost constant ~99% and 120 mAh^{-1} even after 100 cycles. Whereas, for sintered-quenched $Li_{0.48}Nd_{0.5}TiO_3$ (disordered) sample specific capacity reduces from 120 mAh g^{-1} to 100 mAh g^{-1} (~16%) with a retained coulombic efficiency (~99%). In comparison to both the $Li_{0.48}Nd_{0.5}TiO_3$ samples, the specific capacity of $Li_{0.36}Nd_{0.5}TiO_3$ samples are relatively less (110 mAh g^{-1}) with a coulombic efficiency ~99% in the beginning of the charging and discharging. In this sample specific capacity decreased from 110 mAh g^{-1} to 80 mAh g^{-1} (27%).

5.4 Conclusions

This study shows that the order parameter ‘S’ decreases with increasing the Li content (increasing x). With decreasing order parameter S; the degree of orthorhombic distortion decreases. In LiNdTiO ‘S’ varies with the diffusion of the Nd ions between the Nd-rich layer and Nd-poor layers that strongly depend on the cooling conditions. This ordering-disordering at the A-site can be ascribed to the polymorphic phase transformation [19]. Since high temperature is favourable for the diffusion of Nd ions between Nd-rich and Nd-poor layers that increases S value (ordering parameter), as the cooling condition changes, the symmetry of the structure also alters. It was observed that the combined effect of the vacancy and aliovalent substitution slightly distorted the structure to pseudotetragonal (orthorhombic) with very minute difference in a and b lattice parameters ~ a_p x a_p x 2 c_p (3.82 Å x 3.81 Å x 7.68 Å) that still belongs to tetragonal lattice with $P4/mmm$ *or Pmmm* symmetry. Whereas, the crystal structure of a sintered and quenched $Li_{0.48}Nd_{0.5}TiO_3$ sample shows an orthorhombic crystal symmetry (*Pnma*) with $\sqrt{2}a$p x $\sqrt{2}a$p x cp (5.45 Å x 5.36 Å x 7.67 Å). This change in crystal structure is ascribed to the disordering of Nd-ions, Li-ions, and vacancies at A-site cations. During the phase transition material changes the crystal structure and lattice parameters. The decrease in the orthorhombic distortion may be observed as a function of lithium-ion content. The peak positions of XRD patterns was roughly unchanged after Li insertion, referring to a strong integrity of the host structure. These was not significant change observed during the electrochemical lithiation-delithiation. The materials are stable up to 100 charge and discharge cycles. The APT analysis illustrates a 3D compositional phase separation between Li-rich and Li-poor domains. Later these domains take the shape of rods which may facilitate as separate channels for ion flow. It has been observed for CoFeMn oxide that inter-penetration of two sets of mutually perpendicular twins leads to the formation of CB-like microstructure. In case of $LiNdTiO_3$, mutually perpendicular twins along 100 type interfaces leads to the formation of CB-like microstructure. However, it has not happened as extensively as CoFeMn oxide under similar heat treatment conditions. Where ever inter-penetration is not complete, linear strip-like pattern has been observed (Figure 5.6). As the APT needle was lifted off from a randomly chosen position of the sample, CB-like pattern was not observed in APT. However, composition modulation forming linear channels could be observed.

The comparative electrochemical analysis of $Li_{0.48}Nd_{0.5}TiO_3$ samples in sintered-annealed and quenched conditions shows that the voltammograms corresponding to both conditions are symmetric along the horizontal axis. The separation between the main redox peaks (ΔE_p~ 0.2 V) is greater than 57 mV that refers to partial-reversibility of the redox reactions. However, no significant change in the position and shape of the redox peaks was observed after 100 cycles,. The symmetric nature of the voltammograms suggest sufficient structural stability during the charging and discharging cycles. However, a multi-phase refinement of XRD patterns of sintered-annealed $Li_{0.48}Nd_{0.5}TiO_3$ samples after and before running charging and discharging cycles exhibits the actual modification in the crystal structures. The refined XRD pattern of sintered-annealed $Li_{0.48}Nd_{0.5}TiO_3$ sample before running charge and discharge cycles suggests that Nd-ions, Li-ions, are ordered in alternate (001) planes at A-site. The cationic ordering in (001) planes doubles the *c*-parameter of a primitive perovskite structure and turns it into a pseudotetragonal structure with Pmmm space group. On the other hand, similar analysis of sintered-annealed $Li_{0.48}Nd_{0.5}TiO_3$ sample after running charging and discharging cycles shows that this pseudo-tetragonal structure turns orthorhombic perovskite structure with Pnma space group with a_o~5.45 Å, b_o~5.36 Å and c_o~7.67 Å. With the similar electrochemical investigation, the voltammograms of sintered and quenched $Li_{0.48}Nd_{0.5}TiO_3$ sample were also found symmetric along horizontal axis, which denotes adequate structural stability of the material. However, the electrochemical performance (coulombic efficiency and charge capacity) of sintered $Li_{0.48}Nd_{0.5}TiO_3$ sample is comparable to its sintered-annealed counterpart in the beginning, it deteriorates faster. In sintered-quenched $Li_{0.48}Nd_{0.5}TiO_3$ (disordered) sample specific capacity reduces from 120 mAh g^{-1} to 100 mAh g^{-1} (~16%) with a retained coulombic efficiency (~99%). On other hand, the specific capacity and coulombic efficiency of sintered-annealed $Li_{0.48}Nd_{0.5}TiO_3$ sample remain constant at ~99% and 120 mAh^{-1} even after 100 cycles. To investigate the effect of Li content on their electrochemical performances a comparison between $Li_{0.48}Nd_{0.5}TiO_3$ samples, and $Li_{0.36}Nd_{0.5}TiO_3$ samples was performed. This analysis shows that the specific capacity and coulombic efficiency of $Li_{0.36}Nd_{0.5}TiO_3$ samples are relatively less (110 mAh g^{-1}), ~99% from the beginning of the charging and discharging. In this sample specific capacity has drastically decreased from 110 mAh g^{-1} to 80 mAh g^{-1}(27%). This investigation shows a poor structural stability of $Li_{0.36}Nd_{0.5}TiO_3$ during charging-discharging study.

References:

[1] Y. Inaguma, C. Liquan, M. Itoh, T. Nakamura, T. Uchida, H. Ikuta, M. Wakihara, High ionic conductivity in lithium lanthanum titanate, Solid State Commun. 86 (1993) 689–693. https://doi.org/10.1016/0038-1098(93)90841-A.

[2] Y. Inaguma, T. Katsumata, M. Itoh, Y. Morii, Crystal structure of a lithium ion-conducting perovskite $La_{2/3-x}Li_{3x}TiO_3$ (x=0.05), J. Solid State Chem. 166 (2002) 67–72. https://doi.org/10.1006/jssc.2002.9560.

[3] Y. Inaguma, J. Yu, Y. Shan, M. Itoh, T. Nakamuraa, The effect of the hydrostatic pressure on the ionic conductivity in a perovskite lanthanum lithium titanate, J. Electrochem. Soc. 142 (1995) L8–L11. https://doi.org/10.1149/1.2043988.

[4] H. Xu, S. Wang, H. Wilson, F. Zhao, A. Manthiram, Y-Doped NASICON-type $LiZr_2(PO_4)_3$ solid electrolytes for lithium-metal batteries, Chem. Mater. 29 (2017) 7206–7212. https://doi.org/10.1021/acs.chemmater.7b01463.

[5] M. Itoh, Y. Inaguma, W. Jung, L. Chen, T. Nakamura, High lithium ion conductivity in the perovskite-type compounds, Solid State Ionics. 70–71 (1994) 203–207. https://doi.org/10.1016/0167-2738(94)90310-7.

[6] H. Hoppe, N.S. Sariciftci, Morphology of polymer/fullerene bulk heterojunction solar cells, J. Mater. Chem. 16 (2006) 45–61. https://doi.org/10.1039/B510618B.

[7] B.S. Guiton, P.K. Davies, Nano-chessboard superlattices formed by spontaneous phase separation in oxides, Nat. Mater. 6 (2007) 586–591. https://doi.org/10.1038/nmat1953.

[8] B.S. Guiton, P.K. Davies, Spontaneous compositional nanopatterning in Li-containing perovskite oxides, J. Am. Chem. Soc. 130 (2008) 17168–17173. https://doi.org/10.1021/ja806130u.

[9] Y. Harada, Lithium ion conductivity of polycrystalline perovskite $La_{0.67-x}Li_{3x}TiO_3$ with ordered and disordered arrangements of the A-site ions, Solid State Ionics. 108 (1998) 407–413. https://doi.org/10.1016/S0167-2738(98)00070-8.

[10] Y. Inaguma, T. Katsumata, M. Itoh, Y. Morii, T. Tsurui, Structural investigations of migration pathways in lithium ion-conducting $La_{2/3-x}Li_{3x}TiO_3$ perovskites, Solid State Ionics. 177 (2006) 3037–3044. https://doi.org/10.1016/j.ssi.2006.08.012.

[11] A.D. Robertson, S.G. Martin, A. Coats, A.R. West, Phase diagrams and crystal chemistry in the Li^+-ion conducting perovskites, $Li_{0.5-3x}RE_{0.5+x}$ TiO_3 : RE=La, Nd, J. Mater. Chem. 5 (1995) 1405–1412. https://doi.org/10.1039/JM9950501405.

[12] A.M. Abakumov, R. Erni, A.A. Tsirlin, M.D. Rossell, D. Batuk, G. Nénert, G. Van

Tendeloo, Frustrated octahedral tilting distortion in the incommensurately modulated $Li_{3x}Nd_{2/3-x}TiO_3$ Perovskites, Chem. Mater. 25 (2013) 2670–2683. https://doi.org/10.1021/cm4012052.

[13] F. Azough, D. Kepaptsoglou, Q.M. Ramasse, B. Schaffer, R. Freer, On the origin of nanochessboard superlattices in A-site-deficient Ca-Stabilized $Nd_{2/3}TiO_3$, Chem. Mater. 27 (2015) 497–507. https://doi.org/10.1021/cm5036985.

[14] X. Gao, C.A.J. Fisher, T. Kimura, Y.H. Ikuhara, H. Moriwake, A. Kuwabara, H. Oki, T. Tojigamori, R. Huang, Y. Ikuhara, Lithium atom and A-site vacancy distributions in lanthanum lithium titanate, Chem. Mater. 25 (2013) 1607–1614. https://doi.org/10.1021/cm3041357.

[15] S. Stramare, V. Thangadurai, W. Weppner, Lithium lanthanum titanates: A Review, Chem. Mater. 15 (2003) 3974–3990. https://doi.org/10.1021/cm0300516.

[16] Y. Shan, The effect of electrostatic potentials on lithium insertion for perovskite oxides, Solid State Ionics. 79 (1995) 245–251. https://doi.org/10.1016/0167-2738(95)00069-I.

[17] S. García-Martin, F. García-Alvarado, A.D. Robertson, A.R. West, M.A. Alario-Franco, Microstructural study of the Li^+-ion substituted perovskites $Li_{0.5-3x}Nd_{0.5+x}TiO_3$, J. Solid State Chem. 128 (1997) 97–101. https://doi.org/10.1006/jssc.1996.7173.

[18] P.M. Woodward, Octahedral tilting in perovskites. I. Geometrical Considerations, Acta Crystallogr. Sect. B Struct. Sci. 53 (1997) 32–43. https://doi.org/10.1107/S0108768196010713.

[19] M. Nakayama, K. Imaki, Y. Uchimoto, M. Wakihara, Changes in electronic structure upon lithium insertion reaction into the A-site deficient perovskite type oxides, Gd1/3TaO3, Solid State Ionics. 172 (2004) 77–80. https://doi.org/10.1016/j.ssi.2004.04.026.

[20] J.N. Reimers, J.R. Dahn, Electrochemical and in-situ X-Ray diffraction studies of lithium intercalation in Li_xCoO_2, J. Electrochem. Soc. 139 (1992) 2091–2097. https://doi.org/10.1149/1.2221184.